Journal of Materials Chemistry A

RSC Publishing

PAPER

View Article Online
View Journal | View Issue

Cite this: J. Mater. Chem. A, 2013, 1, 6081

Room-temperature synthesis of ZIF-90 nanocrystals and the derived nano-composite membranes for hydrogen separation

Tingxu Yang[ab] and Tai-Shung Chung*[a]

Nanocrystals of ZIF-90 have been synthesized at room temperature through a novel procedure and incorporated into PBI-based nano-composite membranes for hydrogen purification. The physical and chemical structures of the ZIF-90 nanoparticles have been examined *via* multiple advanced instrumental analyses including DLS, XRD, FESEM, NMR and FTIR. The nanocrystals show identical morphology, crystallinity and chemical structure but a significantly reduced particle size (around 100 nm) when compared with the ZIF-90 particles in previous studies. The derived ZIF-90–PBI nano-composite membranes exhibit homogeneous particle dispersion and fine particle–polymer adhesion, as well as excellent hydrogen purification performance at various testing conditions. The 45/55 (w/w) ZIF-90–PBI membrane with the highest ZIF-90 volume loading of up to 50.9 vol% possesses the best ideal H_2–CO_2 separation performance with a moderate H_2 permeability of 24.5 Barrer and a high H_2–CO_2 selectivity of 25.0 in pure gas permeation tests at 35 °C. The membrane also shows promoted gas separation performance during mixed gas tests at 180 °C with an H_2 permeability of 226.9 Barrer and an H_2–CO_2 separation factor of 13.3 that surpasses the latest Robeson upper bound for H_2–CO_2 separation. This work not only expands the field of nano-composite membrane fabrication, but also provides prospects for interdisciplinary research combining nano-science and chemical engineering for clean energy development.

Received 5th March 2013
Accepted 15th March 2013

DOI: 10.1039/c3ta10928c

www.rsc.org/MaterialsA

Introduction

Hydrogen production is a large and fast expanding industry. Currently, the scale of hydrogen production is estimated to be around 500 billion m^3 per year, which is approximately equivalent to 3.3 million barrels of crude oil per day or 10% of the total energy currently consumed for transportation.[1,2] As of 2005, the global market value of hydrogen produced is approximately 135 billion US dollars per year, and the growth rate is about 10% per year.[3] Until now, hydrogen has mostly been consumed for ammonia production and oil refining, and has also been utilized in a wide range of other applications such as chemical production, food processing, metal refining and electronics manufacturing.[4] On the other hand, hydrogen is being considered as a promising energy carrier for future sustainability and energy security due to its cleanness, high energy density, and variety of applications.[5]

Current commercial sources of hydrogen include steam reforming, partial oxidation, water electrolysis, coal gasification, biological hydrogen generation, photodissociation, and thermal splitting of water, *etc.*[4] Specifically, the largest sector of hydrogen production involves steam reforming of hydrocarbons followed by the water–gas shift reaction.[6,7] CO_2 is the main by-product of this process and needs to be captured to meet the hydrogen purity requirement and reduce greenhouse gas emission. Conventional methods for hydrogen and CO_2 separation such as cryogenic distillation, pressure-swing adsorption, and amine-based absorption are energy intensive and not environmental friendly.[8] Recently, membrane based separation technology has shown great promise for gas separation with the advantages of low energy consumption, cleanness, easy operation and small environmental footprint over conventional technologies.[7–12]

The gas permeation mechanism in a polymeric membrane is usually described by the solution-diffusion model,[13] in which the gas pair selectivity is the product of solubility selectivity and diffusion selectivity. For the separation of H_2 and CO_2, the solubility selectivity favors CO_2 transportation due to its higher critical temperature (304 K for CO_2 *vs.* 33 K for H_2) while the diffusion selectivity favors H_2 transportation due to its smaller kinetic diameter (2.89 Å for H_2 *vs.* 3.30 Å for CO_2). As a result, the overall H_2–CO_2 selectivity of a membrane depends on the balance of these two components.

[a]Department of Chemical & Biomolecular Engineering, National University of Singapore, 119260 Singapore, Singapore. E-mail: chencts@nus.edu.sg; Fax: +65 6779 1936; Tel: +65 6874 6645

[b]NUS Graduate School for Integrative Sciences and Engineering, National University of Singapore, 117456 Singapore, Singapore

Generally, membranes made of rubbery polymers are CO_2-selective because of a good CO_2 affinity (*i.e.*, high CO_2–H_2 solubility selectivity) and a high degree of chain flexibility (*i.e.*, low H_2–CO_2 diffusivity selectivity). CO_2-selective membranes possess the advantages of eliminating H_2 recompression, requiring a smaller membrane area, and no performance reduction under CO_2 induced plasticization at high pressures.[14–20] Nevertheless, this type of membrane is only suitable for operating at ambient and low temperatures[7,21] due to the separation mechanism and polymer degradation at high temperatures.

In contrast, membranes derived from glassy polymers are usually H_2-selective because the rigid polymer chains are able to provide a higher H_2–CO_2 diffusion selectivity. H_2-selective membranes possess the advantage of reducing the cost of syngas cooling, water removal, and CO_2 recompression in subsequent sequestration, as well as higher thermal stability and mechanical strength.[7,8,22–30] However, most polymeric materials show insufficient thermal stability and can only be used below 150 °C, thus they are not suitable for high temperature hydrogen purification. For these reasons, glassy polymeric membrane materials with both good H_2–CO_2 separation performance and thermal stability are in high demand for hydrogen separation. Polybenzimidazole (PBI) is one of the promising glassy materials for H_2–CO_2 separation because of its remarkable thermal resistance, superior compression strength and notable intrinsic H_2–CO_2 selectivity.[31–34] However, its low H_2 permeability and brittleness due to rigid and relatively high chain packing limits its broad potential for industrial H_2–CO_2 separation.

Mixed matrix membranes (MMMs) consisting of dispersed inorganic particles in continuous polymer matrices[35–37] have been proposed to overcome the low permeability of PBI while retaining the high H_2–CO_2 selectivity. The particle size and dispersion are critically important for MMM fabrication, especially upon consideration of the industrially favorable membrane configurations (*i.e.*, hollow fibers and spiral wound membranes) with thin selective layers. Since the thickness of these selective layers is usually on the scale of several hundred nanometers, the dimensions of the dispersed particle clusters should be smaller than this in order to take advantage of the separation performance of these particles and to minimize interphase defects and particle penetration. Besides the particle size, the particle synthesis method and the particle–polymer mixing procedure also significantly affect the properties of the resultant MMMs. Preliminary studies have demonstrated that the direct-mixing of as-synthesized wet-state nanoparticles in polymer solutions results in much better particle–polymer adhesion and more uniform particle dispersion than the traditional dry-state mixing method.[38–41]

Recently, zeolitic imidazolate frameworks (ZIF) have been intensively studied as promising candidates for MMM fabrication due to their high intrinsic gas and vapor permeability,[42–47] good chemical and thermal stability[48] and remarkable affinity for polymeric materials.[49] Upon comparing common ZIFs such as ZIF-7 and ZIF-8, ZIF-90 offers more chemical versatility due to the extra aldehyde group on the imidazolate linkers.[50,51] Moreover, experimental[44] and simulation[52] data of ZIF-90 crystalline membranes have indicated superior H_2 permeability, remarkable H_2–CO_2 diffusion selectivity and excellent thermal and steam stabilities of this material, which are beneficial for high temperature H_2–CO_2 separation. Existing ZIF-90 particle synthesis methods include hydrothermal methods, vapor diffusion,[50] and nonsolvent-induced crystallization.[53] These methods produce large particles with sizes from 0.8 μm to 100 μm, and are not suitable for MMM fabrication. The normal room-temperature colloidal chemistry route works well for ZIF-7 (ref. 42) and ZIF-8 (ref. 54–56) particle syntheses, producing nanocrystals with a narrow size distribution between 40 nm and 100 nm. However, for ZIF-90 synthesis, nanocrystals cannot automatically form in the solution at room temperature because the α-hydrogen in the aldehyde group (pK_a near 17) is far more acidic than the C–H bond in the alkyl group (pK_a about 50)[57] thus the reactivity toward ZIF-90 construction is much reduced.

In this work, we report a novel room-temperature synthesis method of nanoscale ZIF-90 particles and demonstrate its applicability by fabricating ZIF-90–PBI nano-composite membranes for hydrogen purification. The resultant membranes show homogeneous particle dispersion, high thermal stability, superior H_2–CO_2 ideal selectivity and high mixed gas separation factors at high temperatures. This study indicates the feasibility of introducing nano-science and nano-technology into advanced materials development for chemical engineering applications.

Experimental

Materials

Polybenzimidazole (PBI) (inherent viscosity of 1.0 dL g^{-1}) was obtained from Hoechst Celanese in the form of a fine powder and the structure of the repeating unit is shown in Fig. 1. The PBI powder was dried at 120 °C under vacuum for 12 h and stored in a dry box prior to use. *N*-Methyl-2-pyrrolidone (NMP) (AR grade, >99.5%), methanol (AR grade, >99.5%) and *n*-hexane (>95.0%) were supplied by Merck. For the synthesis of ZIF-90 nanoparticles, zinc nitrate hexahydrate ($Zn(NO_3)_2 \cdot 6H_2O$) (reagent grade, >98%) and pyridine (anhydrous, 99.8%) were purchased from Sigma-Aldrich. Imidazole-2-carboxyaldehyde (Ica) (>97%) was obtained from Alfa Aesar. *N*,*N*-Dimethylformamide (DMF) (AR grade) was supplied by Fisher. All the reagents and solvents were used as received with no further purification.

Synthesis of ZIF-90 nanoparticles

The crystalline structure image of ZIF-90 from the [111] direction was drawn using Crystal Maker software according to the

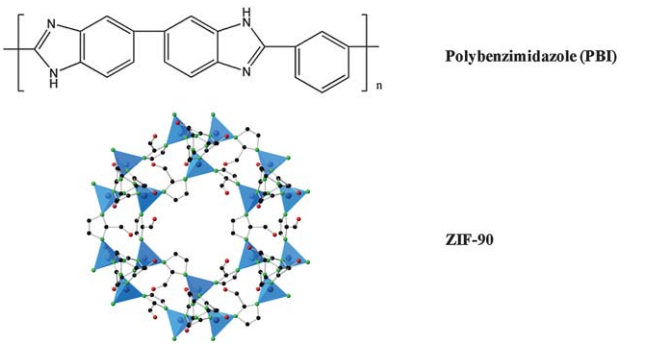

Fig. 1 Chemical structures of PBI and ZIF-90.

Crystallographic Information Framework (CIF) data provided by the literature.[50] Fig. 1 shows the structure of ZIF-90, with tetrahedral Zn sites in blue, N atoms in green, C atoms in black and O atoms in red. H atoms and bonds are omitted for clarity. The well-dispersed ZIF-90 nanocrystals used in this work were synthesized at room temperature using an improved method. Pyridine was added into the synthesis system as a moderate deprotonation agent in order to facilitate ZIF-90 nanocrystal formation in the reaction solution. Specifically, imidazole-2-carboxyaldehyde (Ica) (3.379 g, 35.17 mmol) was dissolved in 200 g of DMF while heating at 60 °C followed by filtering with 1.0 μm PTFE syringe membrane filters. After the Ica solution had been cooled to room temperature, pyridine (2.000 g, 25.28 mmol) was added to it, and it was uniformly mixed. Then, the solution of $Zn(NO_3)_2 \cdot 6H_2O$ (1.309 g, 4.40 mmol) in 200 g of DMF was quickly poured into the mixture of Ica and pyridine under vigorous magnetic stirring. The mixture slowly became turbid and stirring continued overnight to ensure complete reaction. The as-synthesized ZIF-90 nanoparticles were collected by means of centrifugation and then were washed using 50 ml of fresh DMF. After being washed with DMF three times, the particles were re-suspended in about 30 ml of NMP prior to use. The yield of ZIF-90 in this enhanced process was approximately 30% based on the amount of zinc remaining in the nano-composite membranes, which was determined using thermogravimetric analysis (TGA) with air purging.

Membrane fabrication

The ZIF-90–PBI nano-composite membranes were prepared using a typical ring casting method. To prepare the membrane casting solution, 1.5 wt% of dried PBI powder was first dissolved in NMP at 120 °C with continuous stirring for 48 h. The PBI solution was naturally cooled to room temperature and then filtered using a 1.0 μm PTFE syringe membrane prior to use. The filtered PBI solution was mixed with the as-synthesized wet-state ZIF-90 nanoparticles dispersed in NMP according to the desired weight ratio. The ZIF-90–PBI solution was placed in a sonicator for 15 min and then a rolling mixer for 45 min, with three cycles in total. The casting solution was then poured onto a silicon wafer sealed with a metal ring in a vacuum oven. Subsequently, the solution was degassed under vacuum at 45 °C for 1 h, followed by slow solvent evaporation at 75 °C overnight. After cooling to room temperature, the formed membrane was peeled off from the silicon wafer and then vacuum annealed at 200 °C for 24 h. The rates for all the aforementioned heating and cooling steps were fixed at 20 °C h^{-1}. To ensure the full removal of the solvent trapped inside the ZIF-90 cavities, the dried nano-composite membrane was solvent-exchanged with methanol at room temperature on a rolling mixer for 24 h, and subsequently vacuum dried at 120 °C overnight.

The loadings of ZIF-90 in the membrane are indicated as weight and volume percentages and are defined by the following equations:

$$\varphi_W = \frac{W_{particle}}{W_{particle} + W_{polymer}} \times 100\%$$

$$\varphi_V = \frac{V_{particle}}{V_{particle} + V_{polymer}} \times 100\%$$

where φ_W and φ_V are the particle loadings as weight and volume percentages, respectively; $W_{particle}$ and $V_{particle}$ are the weight and volume of the particles, respectively; and $W_{polymer}$ and $V_{polymer}$ are the weight and volume of the polymer, respectively.

Characterization

In order to examine the particle size distribution of the as-synthesized ZIF-90 nanoparticles in the NMP liquid suspension, dynamic light scattering (DLS) analysis was conducted using a Brookhaven 90Plus Particle Size Analyzer operated at 20 °C. The counting rate was around 200 kcps and ten measurements were combined for the final result.

The crystalline structure of the ZIF-90 nanocrystals as well as the ZIF-90–PBI nano-composite membranes was characterized using wide-angle X-ray diffraction (XRD) employing a Bruker D8 series, GADDS X-ray diffractor (General Area Detector Diffraction System, with a Cu X-ray source, wavelength 1.54 Å). For the ZIF-90 nanocrystals, the as-synthesized wet state ZIF-90 particles were solvent exchanged using methanol for 12 h, which was repeated twice, followed by drying in a vacuum oven at 120 °C overnight. For the XRD tests, the dried ZIF-90 powder was pressed into a small pellet, while the ZIF-90–PBI nanocomposite membranes were cut into small pieces, and were immediately tested. The diameters of both the pellet and the membrane pieces were around 5 mm.

The thermal stability of the ZIF-90–PBI nanocomposite membranes was measured by thermogravimetric analysis (TGA) using a TGA 2050 Thermogravimetric Analyzer (TA Instruments). The membrane samples were heated from 25 °C to 800 °C at a heating rate of 20 °C min^{-1} with 100 ml min^{-1} air purging. The weight of zinc oxide remaining at 800 °C was recorded for calculating the weight of ZIF-90 particles in the membranes according to the stoichiometry. The weight reading at 200 °C was taken as the initial weight, in order to eliminate the effect of absorbed water and residual solvent in the samples.

Solid state ^{13}C cross polarization magic angle spinning (CP/MAS) nuclear magnetic resonance (NMR) spectroscopy measurements were made at ambient pressure on a Bruker Avance 400 (DRX400) spectrometer using a standard Bruker magic angle-spinning (MAS) probe with 4 mm (outside diameter) zirconia rotors. Cross-polarization with MAS (CP/MAS) was used to acquire ^{13}C data at 100.62 MHz. The MAS sample-spinning rate was 8 kHz. The ^{13}C chemical shifts were referenced to tetramethylsilane as zero ppm. The chemical structure of the ZIF-90 dry powder was also examined by Fourier transform infrared spectroscopy (FTIR) over a wavenumber range of 800–4000 cm^{-1} using a Bio-Rad FTIR FTS 135 with 10 ml min^{-1} N_2 purging. The ZIF-90 powder was mixed with KBr and was pressed into flat pallets and examined under transmission mode.

The morphologies of the dried ZIF-90 nanoparticles and ZIF-90–PBI nano-composite membranes were observed using field emission scanning electron microscopy (FESEM), JSM-6700F. The membranes were immersed and fractured in liquid N_2 to obtain a cross-sectional view of the nano-composite membrane. All the

samples were coated using a JEOL JFC-1300 Auto Fine Coater (Pt target, 20 mA for 90 s) prior to loading into the FESEM chamber. The thicknesses of the films were around 50 μm, measured by a precision digital tool for film measurements (error ±1 μm).

Gas sorption measurements

To determine the sorption capacity evolution of the ZIF-90–PBI nano-composite membranes, carbon dioxide sorption curves were measured using a Cahn D200 microbalance sorption cell. Detailed specifications of the dual volume sorption cell can be found elsewhere.[58] The membrane samples were measured at 35 °C over a wide pressure range of 0–30 atm. For each sorption curve measurement, about 80 mg of membrane samples were punched into small pieces with diameters of 1 cm and then loaded into a quartz sample bowl. Then the whole system was evacuated for 24 h. During the test, the cell chamber was fed with CO_2 at a certain pressure and the increase in the sample mass at the equilibrium state was recorded. The equilibrium gas sorption capacities were adjusted for the buoyancy force of the samples and empty bowls. Generally, the dual-sorption model was employed to analyze the gas sorption in the glassy polymer, as shown in the following equation:[59]

$$C = C_D + C_H = k_D p + \frac{C_H' b}{1 + bp}$$

where C refers to the sorbed gas concentration in the polymer expressed by gas volume (cm^3) per polymer volume (cm^3), C_D and C_H indicate the concentrations of the gas penetrant sorbed in the Henry sites and Langmuir sites, respectively, k_D refers to the Henry's law constant indicating gas dissolution in the equilibrium-defined polymer, p (atm) is the feed gas pressure in contact with the polymer, C_H' represents the Langmuir capacity of the polymer, and b is the Langmuir affinity parameter representing the affinity of the gas for a Langmuir site. The Langmuir capacity can indicate the amount of excess free volume in a polymer matrix.

The solubility coefficient (S) of a single gas in a glassy polymer is expressed as the equilibrium gas concentration divided by the gas pressure, as shown in the following equation.

$$S = \frac{C}{p} k_D + \frac{C_H' b}{1 + bp}$$

The diffusion coefficient (D) of a single gas in the membrane can be subsequently determined based on the solution-diffusion model[13] as shown below.

$$D = \frac{P}{S}$$

Evaluation of gas separation performance

The pure gas permeation of the membranes was determined using a variable-pressure constant-volume single gas permeation cell. Detailed specifications of the configuration and operating procedure for the permeation cell can be found elsewhere.[60] The pure gas tests were conducted at 35 °C and a feed pressure of 3.5 atm. At a steady state, the rate of pressure increase (dp/dt) was measured and the permeability of each gas was calculated from the following equation:

$$P = \frac{273 \times 10^{10}}{760} \frac{VL}{AT(p_2 \times 76/14.7)} \left(\frac{dp}{dt}\right)$$

where P is the single gas permeability of the membrane in Barrer (1 Barrer = 1×10^{-10} cm^3 (STP) cm (cm^2 s cmHg)$^{-1}$), V represents the downstream reservoir volume (cm^3), L is the membrane thickness (cm), A represents the effective membrane area (cm^2), T is the operating temperature (K) and p_2 indicates the upstream feed pressure (psia). The ideal permselectivity of a membrane for an H_2 and CO_2 gas pair (α_{H_2/CO_2}) was determined using the following equation:

$$\alpha_{H_2/CO_2} = \frac{P_{H_2}}{P_{CO_2}} = \left(\frac{S_{H_2}}{S_{CO_2}}\right) \times \left(\frac{D_{H_2}}{D_{CO_2}}\right)$$

where P_{H_2} and P_{CO_2} represent the pure gas permeability of H_2 and CO_2, respectively, while S_{H_2}/S_{CO_2} and D_{H_2}/D_{CO_2} represent the selectivity components from the solubility and diffusion coefficients of the gas pair, respectively.

Mixed gas permeation tests were performed using a variable-pressure constant-volume mixed gas permeation cell. Detailed descriptions of the setup and operation of the permeation cell can be found elsewhere.[61] The mixed gas tests were conducted from 35 to 180 °C at 7 atm using a binary gas mixture of 50 vol% H_2 and 50 vol% CO_2 as the feed. The permeability of each gas was calculated using the following equations:

$$P_{H_2} = \frac{273 \times 10^{10}}{760} \frac{y_{H_2} VL}{AT(76/14.7)(x_{H_2} p_2)} \left(\frac{dp}{dt}\right)$$

$$P_{CO_2} = \frac{273 \times 10^{10}}{760} \frac{y_{CO_2} VL}{AT(76/14.7)(x_{CO_2} p_2)} \left(\frac{dp}{dt}\right)$$

where P_{H_2} and P_{CO_2} are H_2 permeability and CO_2 permeability, respectively, p_2 represents the pressure (psia) of the upstream feed gas, and x and y represent the molar fractions of each gas on the feed and the permeated sides, respectively.

The separation factor for mixed gas tests is expressed as the mole fraction ratio of H_2 to CO_2 in the downstream gas divided by the mole fraction ratio of H_2 to CO_2 in the upstream gas, as indicated in the following equation:

$$\alpha_{H_2/CO_2} = \frac{P_{H_2}}{P_{CO_2}} = \frac{y_{H_2}/y_{CO_2}}{x_{H_2}/x_{CO_2}}$$

Results and discussion

Characterization of ZIF-90 nanocrystals

In this work, the ZIF-90 nanocrystals were synthesized by a novel method which was specially developed to obtain ZIF-90 particles with a nano-scale particle size. Fig. 2 shows the

apparent particle size distribution after the 3rd centrifugation and dispersion in an NMP solvent obtained using dynamic light scattering (DLS) measurements. About 60 vol% of the ZIF-90 particles are between 85 and 105 nm, while the rest are between 198 and 245 nm.

Fig. 3 shows the FESEM morphology of the ZIF-90 particles and further confirms their size distribution. The particle sizes generally fall within the range 80 to 200 nm and these results are consistent with the DLS results. The as-synthesized ZIF-90 nanoparticles have a typical cubic crystalline morphology, which is similar to the ZIF-90 particles synthesized *via* a hydrothermal method by Morris *et al.*[50] and nonsolvent-induced crystallization by Bae *et al.*[53]

Fig. 4 shows the XRD spectrum between 2.5° and 50° for the dry state ZIF-90 powder. The ZIF-90 nanocrystals exhibit peaks that are well matched to the simulated ZIF-90 XRD pattern in the literature,[50] confirming the successful formation of the ZIF-90 crystalline structure. The structure of the ZIF-90 framework is correlated to the sodalite (SOD) topology of zeolite, and shows extended 3-D networks with large pores of 11.2 Å and small apertures of 3.5 Å in diameter.

Fig. 5 confirms the chemical structure of ZIF-90 using solid state ^{13}C cross polarization magic angle spinning (CP/MAS) NMR. The NMR spectrum displays resonances at 178, 150, and 130 ppm from the aldehyde carbon atom, the 2-carbon atom of the imidazolate ring, and the symmetrically equivalent 4- and 5-carbon atoms of imidazolate ring, respectively.[50] The NMR spectrum is consistent with the expected structure.

Fig. 6 shows the FTIR spectrum of the ZIF-90 dry powder in a KBr pallet tested under transmission mode. The spectrum shows peaks identical with those in a previous report,[50] providing further evidence for the correct chemical structure. The most representative band at 1668 cm^{-1} as indicated by the arrow corresponds to the aldehyde stretch of the imidazole ligands. The weak peaks at 1258, 1095, and 656 cm^{-1} can be attributed to residue solvents inside the cavities.

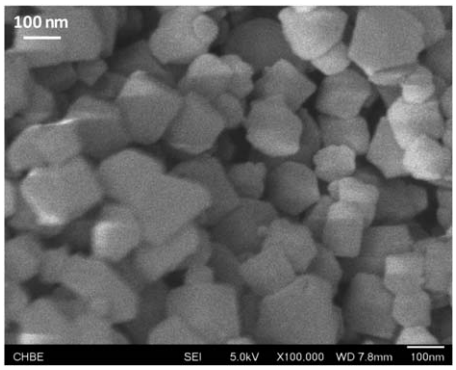

Fig. 3 An FESEM image of the ZIF-90 nanocrystals (dry state powder).

Characterization of the ZIF-90–PBI nano-composite membranes

The weight loadings of ZIF-90 in the nano-composite membranes were measured by TGA analysis under an atmosphere of air. The ash content was obtained from the residual weight of the zinc oxide powder at 800 °C, and the weight of the ZIF-90 nanoparticles was calculated from this according to the stoichiometry. As listed in Table 1, the exact weight loadings of the ZIF-90 nanoparticles in the 10/90 (w/w) ZIF-90–PBI, 25/75 (w/w) ZIF-90–PBI and 45/55 (w/w) ZIF-90–PBI nano-composite membranes were 9.8 wt%, 24.5 wt% and 43.7 wt%, respectively. Subsequently, the volume loadings were estimated from the weight loadings and the density data. According to the literature, the density of PBI is 1.30 g cm^{-3} based on experiments[33] and the density of ZIF-90 is 0.974 g cm^{-3} based on atomically detailed calculations.[52] Thus the volume loadings of the above three membranes were calculated to be 12.7 vol%, 30.2 vol%, and 50.9 vol%, respectively.

Wide-angle XRD measurements between 2.5° and 50° were conducted to determine the crystalline structure inside the 45/55 (w/w) ZIF-90–PBI nano-composite membrane. As shown in Fig. 4, the diffraction pattern of the membrane shows ZIF-90 crystal peaks matching well with the pure ZIF-90 particles,

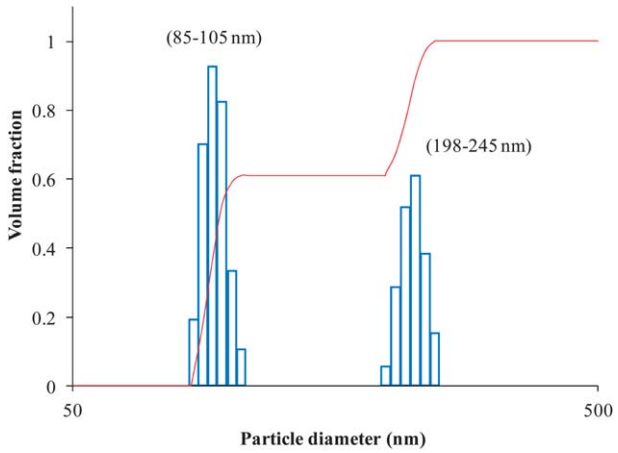

Fig. 2 The particle distribution pattern of the as-synthesized ZIF-90 nanocrystals measured by DLS.

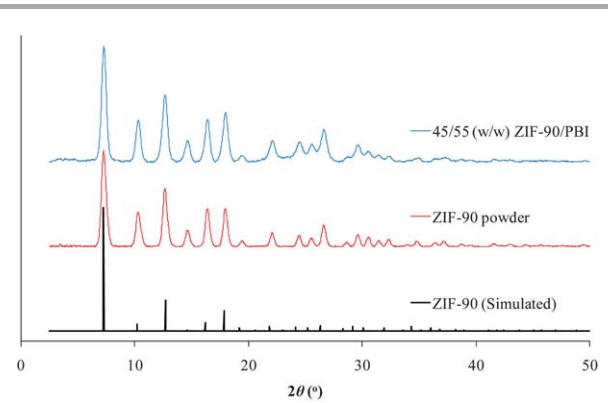

Fig. 4 XRD spectra of the ZIF-90 powder and ZIF-90–PBI nano-composite membrane compared with literature data.

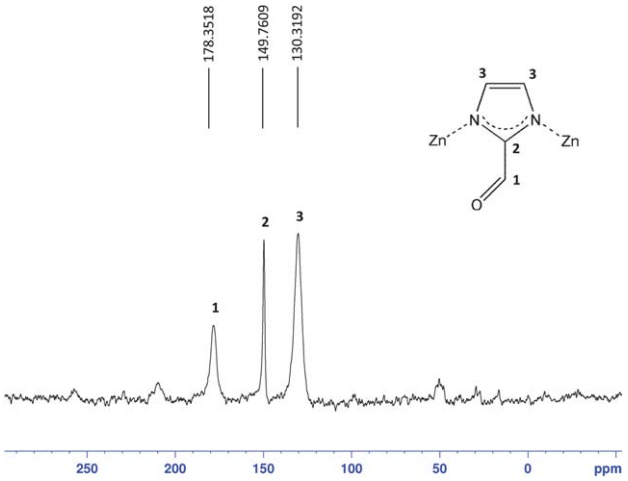

Fig. 5 The solid state ^{13}C CP/MAS NMR spectrum of the ZIF-90 nanocrystals.

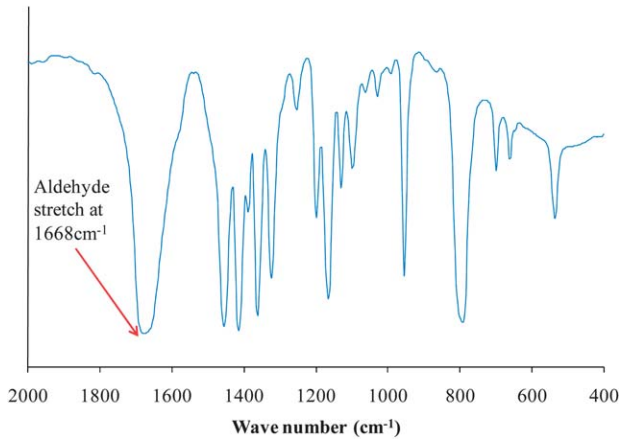

Fig. 6 The FTIR spectrum of the pure ZIF-90 powder.

Table 1 ZIF-90 particle loadings of the nano-composite membranes determined from TGA

Sample ID	Ash content weight (%)	ZIF-90 weight (%)	ZIF-90 volume (%)
Pure PBI	0	0	0
10/90 (w/w) ZIF-90–PBI	3.1	9.8	12.7
25/75 (w/w) ZIF-90–PBI	7.8	24.5	30.2
45/55 (w/w) ZIF-90–PBI	13.9	43.7	50.9

indicating that the ZIF-90 crystalline structure remained unchanged after being incorporated into the PBI matrix.

Field emission scanning electron microscopy (FESEM) measurements were conducted on the ZIF-90–PBI membrane with the highest ZIF-90 loading to determine the particle dispersion state. Fig. 7 clearly shows that the ZIF-90 nanoparticles are uniformly dispersed in the 45/55 (w/w) ZIF-90–PBI membrane. At a magnification of $\times$100 000 neither particle agglomeration nor interphase voids can be observed in this membrane. This homogeneously dispersed morphology proves the excellent interphase affinity between ZIF-90 nanoparticles and the PBI polymer matrix, and also indicates the feasibility of fabricating defect-free asymmetric hollow fibers and thin film composite membranes using the ZIF-90–PBI nano-composite material.

Pure gas transport properties at ambient temperature

The single-gas permeability and ideal selectivity for H_2 and CO_2 of the ZIF-90–PBI nano-composite membranes were measured at 35 °C with a 3.5 atm trans-membrane pressure and the results are listed in Table 2. Both H_2 permeability and H_2–CO_2 ideal selectivity show significant improvements with increasing ZIF-90 loading. In particular, the 45/55 (w/w) ZIF-90–PBI membrane with the highest ZIF-90 loading shows the best performance with an H_2 permeability of 24.5 Barrer and an H_2–CO_2 ideal selectivity of 25.0. The increase in the H_2 permeability is due to the high porosity of the ZIF-90 particles and the sub-nano transportation channels formed at the PBI–ZIF interphase.[38] Compared with previous studies on ZIF-8–PBI nano-composite membranes,[39,40] the ZIF-90–PBI membranes show extremely high ideal selectivity, mainly for the following reasons: (1) ZIF-90 exhibits a much higher H_2–CO_2 diffusion selectivity according to the atomically detailed simulation results;[52] and (2) the aldehyde group in ZIF-90 is more acidic in its enolate form[62] and thus interacts with the N-3 atom on the PBI imidazole ring, which exhibits alkalinity.[63] The enhancements in both the permeability and selectivity become more notable with increased ZIF-90 loading because of superior particle dispersion in the polymer matrix.

To understand the contributions of the solubility and diffusivity changes to the overall permeability, CO_2 sorption curves for pure PBI and the ZIF-90–PBI nano-composite membranes were measured at 35 °C from 0 to 30 atm. Fig. 8 shows the sorption curves, and Table 3 lists the relative transportation parameters calculated from the sorption results. In comparison with pure PBI, the ZIF-90–PBI membranes exhibit an enhancement in CO_2 solubility such that it is increased approximately threefold because of the high

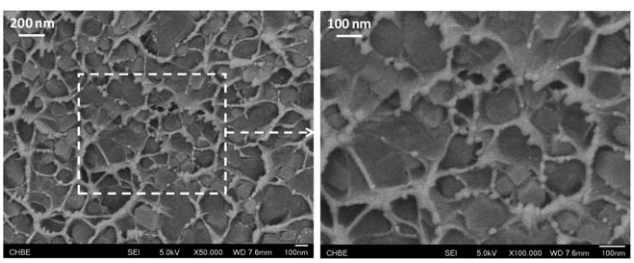

Fig. 7 FESEM images of the 45/55 (w/w) ZIF-90–PBI nano-composite membrane.

Table 2 Pure gas separation performance of pure PBI and the ZIF-90–PBI nano-composite membranes at 35 °C

Sample ID	ZIF-90 weight%	Permeability[a] (Barrer[b])		
		H_2	CO_2	Selectivity (H_2–CO_2)
Pure PBI	0	4.1 ± 0.1	0.46 ± 0.01	8.9 ± 0.2
10/90 (w/w) ZIF-90–PBI	9.8	12.7 ± 0.7	0.87 ± 0.06	14.6 ± 0.3
25/75 (w/w) ZIF-90–PBI	24.5	18.3 ± 0.4	0.89 ± 0.09	20.6 ± 1.7
45/55 (w/w) ZIF-90–PBI	43.7	24.5 ± 0.5	0.98 ± 0.24	25.0 ± 4.9

[a] Single gas tests were performed at 3.5 atm, at 35 °C. [b] 1 Barrer = 1×10^{-10} cm^3 (STP) cm (cm^2 s cmHg)$^{-1}$.

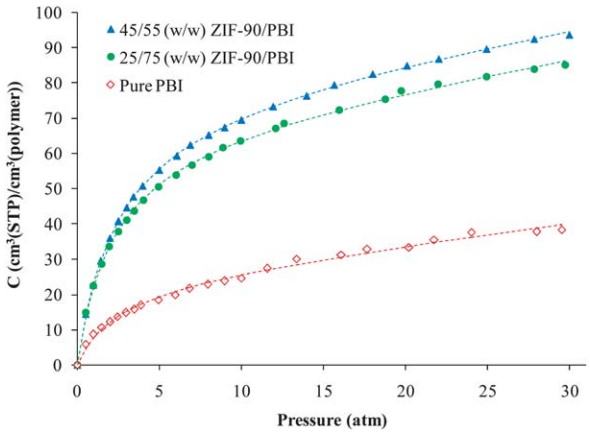

Fig. 8 CO_2 sorption isotherms of pure PBI and ZIF-90–PBI nano-composite membranes.

porosity and CO_2 adsorption capacity of the ZIF-90 particles.[50,52] However, the diffusivity of CO_2 decreases slightly in the ZIF-90–PBI nano-composite membranes. This decrease phenomenon is unique because other ZIF based nano-composite materials usually show an increase in CO_2 diffusivity with increasing ZIF loading.[40,41,64,65] The reduction in the CO_2 diffusivity may indicate a narrowing of gas transport pathways due to the special interaction between the ZIF-90 particles and the PBI chains.

Mixed gas performance at high temperatures

Fig. 9 shows the mixed gas permeation results of the 45/55 (w/w) ZIF-90–PBI membrane from 35 to 180 °C using a 50/50 (mol/mol) H_2–CO_2 binary gas mixture as the feed gas. At 35 °C, the membrane obviously shows a reduced gas selectivity compared with the pure gas data. This phenomenon may be due to plasticization by the more condensable component (CO_2 in this study) and competitive sorption.[66–68] The CO_2 in the gas mixture may plasticize the membrane, decrease the diffusivity selectivity, and decrease the gas pair selectivity. Both H_2 permeability and H_2–CO_2 selectivity increase significantly with an increase in temperature. At 180 °C, the membrane shows an impressive mixed gas separation performance with an H_2 permeability of 226.9 Barrer and an H_2–CO_2 separation factor of 13.3.

The permeation of H_2 or CO_2 across the ZIF-90–PBI membranes is a thermally activated process. The temperature dependence of gas permeability can be described by the Arrhenius–van't Hoff equation:[66]

$$P = P_0 \exp\left(\frac{-E_p}{RT}\right)$$

where P represents the gas permeability, P_0 represents the pre-exponential coefficient, E_p represents the apparent activation energy in the permeation process, R is the gas constant, and T stands for the absolute temperature. Based on the solution-diffusion model, E_p can be expressed in terms of two contributions:

$$E_p = E_D + \Delta H_S$$

where E_D represents the activation energy of diffusion and is always positive, while ΔH_S represents the enthalpy of sorption and is usually negative. For strongly size-sieving membranes, E_D is larger than the absolute value of ΔH_S, thus the total value E_p is positive and the gas permeability increases as the temperature increases.

Fig. 10 shows the temperature dependence of individual gas permeability (P) across the 45/55 (w/w) ZIF-90–PBI nano-composite membrane by means using the Arrhenius–van't Hoff equation and mixed gas data. The activation energies (E_p) of H_2 and CO_2 permeation through the 45/55 (w/w) ZIF-90–PBI membrane are 15.4 and 8.4 kJ mol^{-1}, respectively, indicating a strong size-sieving effect for both H_2 and CO_2 gas molecules, which is consistent with the results of the diffusion coefficients.

Table 3 P, D and S coefficients of CO_2 in pure PBI and ZIF-90–PBI nano-composite membranes at 35 °C and 3.5 atm

Sample ID	Permeability (Barrer)	Solubility (cm^3 (STP)/cm^3 atm)	Diffusivity ($\times 10^8$ cm^2 s^{-1})
Pure PBI	0.46	4.65	0.0753
25/75 (w/w) ZIF-90–PBI	0.89	12.52	0.0541
45/55 (w/w) ZIF-90–PBI	0.98	13.84	0.0539

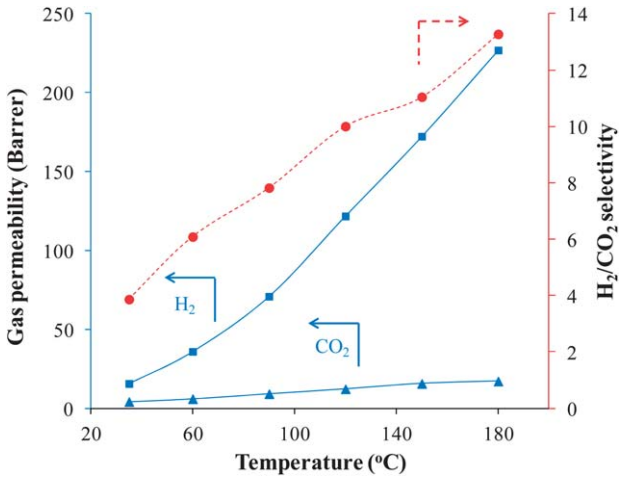

Fig. 9 H_2–CO_2 mixed gas permeation results for the ZIF-90–PBI nano-composite membranes.

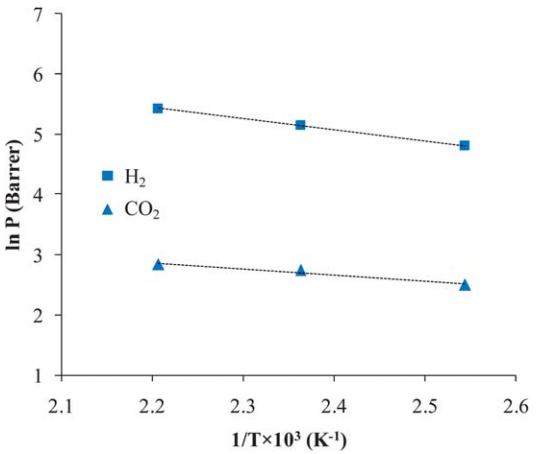

Fig. 10 Temperature dependence of gas permeability (P) in the 45/55 (w/w) ZIF-90–PBI nano-composite membrane.

The activation energy of CO_2 permeation is lower than that of H_2 because CO_2 exhibits a far more negative enthalpy of sorption (ΔH_S) in the membrane. As a result, the H_2 permeability increases faster than that for CO_2 as the temperature increases, thus the H_2–CO_2 selectivity becomes higher with increasing temperature. The gas separation performance of the 45/55 ZIF-90–PBI membrane at 400 °C can be therefore predicted from their individual activation energies and gas permeabilities at 180 °C. The predicted H_2 permeability is 864.6 Barrer while the calculated H_2–CO_2 selectivity is 23.8 at 400 °C.

Fig. 11 compares the pure gas and mixed gas permeation results of the 45/55 ZIF-90–PBI nano-composite membrane with the latest Robeson upper bound[69] for H_2–CO_2 separation. The ideal H_2 permeability and H_2–CO_2 selectivity at 35 °C of the 45/55 (w/w) ZIF-90–PBI has surpassed the upper bound. Although the mixed gas result at 35 °C drops significantly compared with the pure gas results, an encouraging performance recovery is shown when the membrane is tested with mixed gases at elevated temperatures.

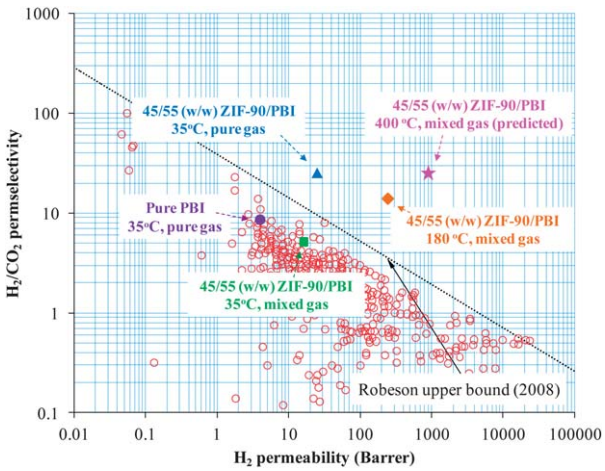

Fig. 11 H_2–CO_2 separation performance of ZIF-90–PBI nano-composite membranes compared to the Robeson upper bound: ● pure PBI, 35 °C, pure gas; ▲ 45/55 (w/w) ZIF-90–PBI, 35 °C, pure gas; ■ 45/55 (w/w) ZIF-90–PBI, 35 °C, mixed gas; ◆ 45/55 (w/w) ZIF-90–PBI, 180 °C, mixed gas; ★ 45/55 (w/w) ZIF-90–PBI, 400 °C, mixed gas (predicted).

Conclusions

In this work, we have successfully synthesized ZIF-90 nanocrystals *via* a specially designed route in order to keep the particles small and maximize the separation performance of ZIF-90–PBI nano-composite membranes for H_2–CO_2 separation. Investigations on the properties of the ZIF-90 nanoparticles and the derived nano-composite membranes were carried out using advanced instrumental analysis and gas permeation tests. The following conclusions can be made from this study.

(1) Compared with the ZIF-90 particles in previous studies, the ZIF-90 nanoparticles in this study exhibit identical morphology, crystallinity and chemical structure, but with a significantly reduced particle size (around 100 nm). As a result, no visible particle agglomeration is observed and the derived ZIF-90–PBI nano-composite membranes possess homogeneous particle dispersion and fine particle–polymer adhesion as observed by FESEM.

(2) The incorporation of ZIF-90 nanoparticles into PBI-based membranes increases CO_2 solubility coefficients while reducing CO_2 diffusion coefficients. This transition may indicate an increased H_2–CO_2 diffusion selectivity which explains the enhancement of the ideal H_2–CO_2 selectivity. The 45/55 (w/w) ZIF-90–PBI membrane achieves the highest ZIF-90 volume loading of up to 50.9 vol%. This membrane possesses the best ideal H_2–CO_2 separation performance with a moderate H_2 permeability of 24.5 Barrer and a high H_2–CO_2 selectivity of 25.0 in pure gas permeation tests at 35 °C.

(3) Mixed gas permeation results show that the 45/55 (w/w) ZIF-90–PBI membrane suffers a significant performance drop, possibly due to competitive sorption and plasticization phenomena in strongly size-sieving glassy polymeric membranes. Nevertheless, the membrane still possesses an impressive mixed gas separation performance with an H_2 permeability of 226.9 Barrer and an H_2–CO_2 separation factor of

13.3 at 180 °C. Based on activation energy calculations, the membrane may have an H_2 permeability of 864.6 Barrer and an H_2–CO_2 selectivity of 23.8 at 400 °C. The experimental and calculated mixed gas data for the 45/55 ZIF-90–PBI nanocomposite membrane surpass the latest Robeson upper bound for H_2–CO_2 separation.

Acknowledgements

The authors would like to acknowledge the Singapore National Research Foundation (NRF) for the financial support on the Competitive Research Programme for the projects "Molecular Engineering of Membrane Material Research and Technology for Energy Development: Hydrogen, Natural Gas and Syngas" (grant number R-279-000-261-281) and "New Biotechnology for Processing Metropolitan Organic Wastes into Value-Added Products" (grant number: R-279-000-311-281). Special thanks are due to Ms Huan Wang and Dr Dave W. Mangindaan for their valuable suggestions.

Notes and references

1 J. W. Sheffield, in *Assessment of Hydrogen Energy for Sustainable Development*, ed. J. W. Sheffield and C. Sheffield, Springer, Dordrecht, 2007, ch. 1, pp. 1–8.
2 J. Conti and P. Holtberg, *International Energy Outlook 2011*, U.S. Energy Information Administration, Washington, 2011.
3 http://www.reporter.leeds.ac.uk/press_releases/current/biodiesel.htm, accessed 3 November 2012.
4 B. Sorensen, *Hydrogen and Fuel Cells*, Elsevier, Burlington, 2nd edn, 2012.
5 N. Armaroli and V. Balzani, *Energy for A Sustainable World*, Wiley-VCH, Weinheim, 2011.
6 T. Abbasi and S. A. Abbasi, *Renewable Sustainable Energy Rev.*, 2011, **15**, 3034.
7 T. C. Merkel, M. Zhou and R. W. Baker, *J. Membr. Sci.*, 2012, **389**, 441.
8 L. Shao, B. T. Low, T. S. Chung and A. R. Greenberg, *J. Membr. Sci.*, 2009, **327**, 18.
9 S. A. Stern, *J. Membr. Sci.*, 1994, **94**, 1.
10 P. Bernardo, E. Drioli and G. Golemme, *Ind. Eng. Chem. Res.*, 2009, **48**, 4638.
11 N. W. Ockwig and T. M. Nenoff, *Chem. Rev.*, 2007, **107**, 4078.
12 R. W. Baker, *Ind. Eng. Chem. Res.*, 2002, **41**, 1393.
13 J. H. Petropoulos, in *Polymeric gas separation membranes*, ed. D. R. Paul and Y. P. Yampol'skii, CRC Press, Boca Raton, 1994, ch. 2, pp. 17–81.
14 M. Kawakami, H. Iwanaga, Y. Hara, M. Iwamoto and S. Kagawa, *J. Appl. Polym. Sci.*, 1982, **27**, 2387.
15 H. Lin, E. Van Wagner, B. D. Freeman, L. G. Toy and R. P. Gupta, *Science*, 2006, **311**, 639.
16 L. Shao and T. S. Chung, *Int. J. Hydrogen Energy*, 2009, **34**, 6492.
17 H. Z. Chen, Y. C. Xiao and T. S. Chung, *Polymer*, 2010, **51**, 4077.
18 A. Car, C. Stropnik, W. Yave and K. V. Peinemann, *Sep. Purif. Technol.*, 2008, **62**, 110.
19 J. Xia, S. Liu, C. H. Lau and T. S. Chung, *Macromolecules*, 2011, **44**, 5268.
20 C. H. Lau, S. Liu, D. R. Paul, J. Xia, Y. C. Jean, H. Chen, L. Shao and T. S. Chung, *Adv. Energy Mater.*, 2011, **1**, 634.
21 R. D. Raharjo, B. D. Freeman, D. R. Paul, G. C. Sarti and E. S. Sanders, *J. Membr. Sci.*, 2007, **306**, 75.
22 L. Shao, J. Samseth and M. B. Hägg, *J. Membr. Sci.*, 2009, **326**, 285–292.
23 Y. Liu, R. Wang and T. S. Chung, *J. Membr. Sci.*, 2001, **189**, 231.
24 J. D. Wind, C. Staudt-Bickel, D. R. Paul and W. J. Koros, *Macromolecules*, 2003, **36**, 1882.
25 C. H. Lau, B. T. Low, L. Shao and T. S. Chung, *Int. J. Hydrogen Energy*, 2010, **35**, 8970.
26 B. T. Low, Y. C. Xiao, T. S. Chung and Y. Liu, *Macromolecules*, 2008, **41**, 1297.
27 L. Shao, C. H. Lau and T. S. Chung, *Int. J. Hydrogen Energy*, 2009, **34**, 8716.
28 B. T. Low, T. S. Chung, H. Chen, Y. C. Jean and K. P. Pramoda, *Macromolecules*, 2009, **42**, 7042.
29 B. T. Low, Y. C. Xiao and T. S. Chung, *Polymer*, 2009, **50**, 3250.
30 C. E. Powell, X. J. Duthie, S. E. Kentish, G. G. Qiao and G. W. Stevens, *J. Membr. Sci.*, 2007, **291**, 199.
31 T. S. Chung, *J. Macromol. Sci., Rev. Macromol. Chem. Phys.*, 1997, **37**, 277.
32 T. S. Chung and Z. L. Xu, *J. Membr. Sci.*, 1998, **147**, 35.
33 S. C. Kumbharkar, P. B. Karadkar and U. K. Kharul, *J. Membr. Sci.*, 2006, **286**, 161.
34 S. S. Hosseini, M. M. Teoh and T. S. Chung, *Polymer*, 2008, **49**, 1594.
35 S. Choi, J. Coronas, Z. Lai, D. Yust, F. Onorato and M. Tsapatsis, *J. Membr. Sci.*, 2008, **316**, 145.
36 T. S. Chung, L. Y. Jiang, Y. Li and S. Kulprathipanja, *Prog. Polym. Sci.*, 2007, **32**, 483.
37 T. Yang, Y. C. Xiao and T. S. Chung, *Energy Environ. Sci.*, 2011, **4**, 4171.
38 G. M. Shi, T. Yang and T. S. Chung, *J. Membr. Sci.*, 2012, **415**, 577.
39 T. Yang, G. M. Shi and T. S. Chung, *Adv. Energy Mater.*, 2012, **2**, 1358.
40 T. Yang and T. S. Chung, *Int. J. Hydrogen Energy*, 2013, **38**, 229.
41 Q. Song, S. K. Nataraj, M. V. Roussenova, J. C. Tan, D. J. Hughes, W. Li, P. Bourgoin, M. A. Alam, A. K. Cheetham, S. A. Al-Muhtaseb and E. Sivaniah, *Energy Environ. Sci.*, 2012, **5**, 8359.
42 Y. S. Li, F. Y. Liang, H. Bux, A. Feldhoff, W. S. Yang and J. Caro, *Angew. Chem., Int. Ed.*, 2010, **49**, 548.
43 A. Huang, H. Bux, F. Steinbach and J. Caro, *Angew. Chem., Int. Ed.*, 2010, **49**, 4958.
44 A. Huang, W. Dou and J. Caro, *J. Am. Chem. Soc.*, 2010, **132**, 15562.
45 S. R. Venna and M. A. Carreon, *J. Am. Chem. Soc.*, 2010, **132**, 76.
46 G. M. Shi, H. M. Chen, Y. C. Jean and T. S. Chung, *Polymer*, 2013, **54**, 774.

47 Y. Pan and Z. P. Lai, *Chem. Commun.*, 2011, **47**, 10275.
48 K. S. Park, Z. Ni, A. P. Côté, J. Y. Choi, R. Huang, F. J. Uribe-Romo, H. K. Chae, M. O'Keeffe and O. M. Yaghi, *Proc. Natl. Acad. Sci. U. S. A.*, 2006, **103**, 10186.
49 J. Caro, *Curr. Opin. Chem. Eng.*, 2011, **1**, 77.
50 W. Morris, C. J. Doonan, H. Furukawa, R. Banerjee and O. M. Yaghi, *J. Am. Chem. Soc.*, 2008, **130**, 12626.
51 A. Huang and J. Caro, *Angew. Chem., Int. Ed.*, 2011, **50**, 4979.
52 E. Atci and S. Keskin, *J. Phys. Chem. C*, 2012, **116**, 15525.
53 T. H. Bae, J. S. Lee, W. Qiu, W. J. Koros, C. W. Jones and S. Nair, *Angew. Chem., Int. Ed.*, 2010, **49**, 9863.
54 J. Cravillon, S. Münzer, S. J. Lohmeier, A. Feldhoff, K. Huber and M. Wiebcke, *Chem. Mater.*, 2009, **21**, 1410.
55 S. R. Venna, J. B. Jasinski and M. A. Carreon, *J. Am. Chem. Soc.*, 2010, **132**, 18030.
56 M. Zhu, S. R. Venna, J. B. Jasinski and M. A. Carreon, *Chem. Mater.*, 2011, **23**, 3590.
57 F. A. Carey and R. J. Sundberg, *Advanced Organic Chemistry Part B: Reactions and Synthesis*, Springer Science+Business Media, New York, 2007.
58 R. Wang, C. Cao and T. S. Chung, *J. Membr. Sci.*, 2002, **198**, 259.
59 W. J. Koros, G. K. Fleming, S. M. Jordan, T. H. Kim and H. H. Hoehn, *Prog. Polym. Sci.*, 1988, **13**, 339.
60 W. H. Lin, R. H. Vora and T. S. Chung, *J. Polym. Sci., Part B: Polym. Phys.*, 2000, **38**, 2703.
61 L. Shao, T. S. Chung, S. H. Goh and K. P. Pramoda, *J. Membr. Sci.*, 2005, **256**, 46.
62 A. Burrows, J. Holman, A. Parsons, G. Pilling and G. Price, *Chemistry^3: Introducing Inorganic, Organic and Physical Chemistry*, Oxford University Press, Oxford, 2009.
63 X. Zhang and J. Jiang, in *Rare Earth Coordination Chemistry: Fundamentals and Applications*, ed. C. H. Huang, John Wiley & Sons (Asia) Pte Ltd, Singapore, 2010, ch. 4, pp. 137–192.
64 K. Díaz, L. Garrido, M. López-González, L. F. Del Castillo and E. Riande, *Macromolecules*, 2010, **43**, 316.
65 K. Díaz, M. López-González, L. F. Del Castillo and E. Riande, *J. Membr. Sci.*, 2011, **383**, 206.
66 S. Matteucci, Y. Yampolskii, B. D. Freeman and I. Pinnau, in *Materials Science of Membranes for Gas and Vapor Separation*, ed. Y. Yampolskii, I. Pinnau and B. D. Freeman, John Wiley & Sons, Ltd, Chichester, 2006, ch. 1, pp. 1–47.
67 C. Staudt-Bickel and W. J. Koros, *J. Membr. Sci.*, 1999, **155**, 145.
68 L. S. White, T. A. Blinka, H. A. Kloczewski and I. F. Wang, *J. Membr. Sci.*, 1995, **103**, 73.
69 L. M. Robeson, *J. Membr. Sci.*, 2008, **320**, 390.

